Progress In Electromagnetics Research, Vol. 109, 361–379, 2010

ELECTRODYNAMICAL CHARACTERISTIC PARTICULARITY OF OPEN METAMATERIAL SQUARE AND CIRCULAR WAVEGUIDES

T. Gric, L. Nickelson†, and S. Asmontas

Semiconductor Physics Institute
Center for Physical Sciences and Technology
Vilnius, Lithuania

Abstract—We present here the solution of the eigenvalue problems for the open metamaterial square and circular rod waveguides. The Maxwell's equations for the electrodynamical analysis of the open waveguides were solved by the Singular Integral Equations' (SIE) method and partial area method. Our SIE method is pretty universal and let us rigorously analyze open waveguides electrodynamically with any arbitrary cross-sections taking into account of the edge condition. The false roots did not occur applying the SIE method. The waveguide media can be of strongly lossy materials. The signs of the complex permittivity and permeability can be positive or negative in different combinations. We used our computer algorithms based on the two mentioned methods with 3D graphical visualization in the MATLAB language. We present here our numerical calculations of the metamaterial square waveguide with sides equal to $5 \cdot 10^{-3}$ m and the metamaterial circular waveguide with the diameter equal to $5 \cdot 10^{-3}$ m. We present dependences of phase constant and attenuation constant of metamaterial waveguides at the frequency range from 75 GHz till 115 GHz. We have compared the three dimension (3D) electric field distributions of the main mode and the first higher mode propagating in the square and circular metamaterial waveguides. The calculations of the electric fields were fulfilled at approximately 10000 points in every cross-section. We discovered that the electric field is concentrated at the waveguide boundary. The distribution of the electric field along the perimeter of the waveguide is not uniform. There are two areas on the perimeter of the square and circular waveguides

Received 25 August 2010, Accepted 17 October 2010, Scheduled 27 October 2010
Corresponding author: Liudmila Nickelson (lucynickelson@gmail.com).
† L. Nickelson is also with Electronics Faculty, Vilnius Gediminas Technical University, Lithuania.

where the electric field has maximum values. These areas are shifted relative to each other on π radians.

1. INTRODUCTION

Large stream of articles on investigations of waveguide structures made from novel materials points that there is a need for development devices possessing unique characteristics, as multifunctionality, reconfigurability, superwide frequency bandwidth, ability to operate at high-temperatures, high-powers and high-radiation conditions. In order to create a new microwave device it is necessary to know the main electrodynamical characteristics of waveguide on the basis of which the device is supposed to be created. The main characteristics are the phase and attenuation (losses) constants of the main and higher waveguide modes, frequency bandwidth, distribution of electric or (and) magnetic fields. Knowledge about the electric or (and) magnetic field distribution lets us properly excite a desired mode in a waveguide. In addition, the field distribution becomes important to solve the problems about the active interaction between devices that are in the vicinity with each other, including issues of compatibility.

The technological potential of metamaterials for developing novel devices offers a very promising alternative that could potentially overcome the limitations of current technology. The metamaterial waveguides can operate as different devices. In article [1], the characteristics of phase modulator that is created on the base of a metamaterial planar slab are presented. In [2], the metamaterial anomalous behaviors and the potential utilization of metamaterial exotic properties in many electromagnetic applications are described. In [3], the modified open metamaterial waveguide radiator with abnormal antenna pattern diagram and the maximal radiation in the backside direction is demonstrated. A controllable metamaterial absorbing structure is presented in [4].

The complete review of articles on the electromagnetic theory and recent progress in the metamaterials with simultaneously negative permittivities and permeabilities is given in [5]. The authors examined literature about electromagnetics and physics of metamaterials and metamaterial structures, including the aspects of wave propagation in waveguides. There are explanations of three waveguide cases when the propagating modes' transverse wavenumber outside and inside of metamaterial waveguide is real, imaginary or complex number. It is noted that solutions with the complex transverse wavenumber also exist but the wave propagates along the guide with some losses [5].

A number of articles that are devoted to the study of EM wave

propagation in the metamaterial waveguides are limited. Articles in which the most consistently investigated metamaterial waveguides can be presented [6–12]. In [6], theoretical analysis of two layered 1D slab waveguides when materials have the constitutive parameters with signs of all combinations, i.e., with negative real permittivity, but positive real permeability (epsilon-negative (ENG)); with negative real permeability, but positive real permittivity (mu-negative (MNG)); with both negative real permittivity and permeability (double-negative (DNG)), and conventional material with both positive real permittivity and permeability (double-positive (DPS)) are presented. There are dispersion equations and diagrams for the transverse electric (TE) and transverse magnetic (TM) modes dependent on the layer thicknesses and layer material constitutive parameters in the article. The calculations were fulfilled for lossless materials. In [7], dispersion characteristics of the 1D slab waveguides of lossless DPS and DNG materials were investigated and compared. In the article, the TM_m modes with $m = 0, 1, 2 \ldots 5$ are analyzed.

Mode analysis in 1D asymmetric slab waveguides of DNG metamaterial is given in [8]. The slab metamaterial waveguide is surrounded by the different dielectric materials from the top and the bottom. The metamaterial permittivity and permeability were independent on the frequency and are taken equal to -2. The dispersion characteristics' dependencies are analyzed on the normalized frequency, propagation constant and the rations of the surrounding waveguide material permittivities. Dispersion dependencies of TE_m modes at the index m = 1–4 and the surface wave modes are investigated. There are distributions of electric field $E_y(x)$ component of TE_1, TE_2, TE_3 modes. The power flux along the transverse profile of the DNG asymmetric waveguide is also shown in [8]. Articles [9, 10] focused on investigations of the grounded metamaterial waveguides. In [9], dispersion equations of such a waveguide are obtained. The solution dependent on the normalized frequency, thickness of the infinite plate and the constitutive parameters of materials is given. There are two tables with investigations of TE and TM modes. Ref. [10] presented the relative phase constant and the power of TE_0, TE_1, TM_1, TM_2 modes. In [11], wave propagations in a 2D planar dielectric waveguide covered by the MNG metamaterial layers were considered. Here the waveguide thickness when the forward and backward modes can propagate was theoretically found. The waveguide can support TE modes, which were analyzed in the article. In [12], the TE modes propagation through a 1D slab waveguide of uniaxial anisotropic dispersive metamaterial was shown. In the article, the solution of problem, guidance conditions and dispersion

characteristics for bulk TE_2, TE_4, TE_6 and surface modes dependent on the operating frequency and the thickness of metamaterial slab waveguide were given.

It is interesting to note that the authors of [6–12] indicated that transverse TE_m, TM_m and surface modes can only propagate in the examined 1D and 2D isotropic and uniaxial anisotropic metamaterial waveguides. It means that the longitudinal components of EM waves are equal to zero. The waveguide metamaterial structures can possess some unique properties and be used for the development of state-of-the-art microwave devices [13–18].

Here, we present the investigations of the 2D open metamaterial square and circular waveguides. In the present work, we have used the SIE method to analyze the rectangular waveguides and the partial area method to investigate the circular waveguides. We have created computer software to make the electrodynamical analysis of the lossy waveguides. We carried out the testing of our algorithms by comparing our calculations with data from other authors' articles. One of these comparisons is given in [19].

We would like to draw your attention to the fact that the hybrid waves propagate in our investigated metamaterial waveguides. This statement is supported by the table data in the present work. The transverse wavenumbers outside and inside of the metamaterial waveguides are complex numbers because the longitudinal propagation constants of eigenmodes have complex values. It is also important to note that we tried to simulate an electrodynamical situation which would be close to practice. Therefore, we took constitutive parameters of the metamaterial from the experimental data of article [20]. In [20], the metamaterial complex values of permittivities and permeabilities at the frequency range from 75 GHz to 115 GHz are given. For this reason, we have numerically investigated the metamaterial waveguides at the same frequency range.

We have discovered several particularities in the dispersion characteristics of metamaterial waveguides as well as in their field distributions. These specific metamaterial waveguide behaviors can be used in various technical microwave applications. Our research results are described in Sections 2 and 3 of the present article.

2. INVESTIGATIONS OF THE SQUARE WAVEGUIDE BY THE SIE METHOD

Here the metamaterial square rod waveguide with sizes $(5 \times 5) \cdot 10^{-3}$ m is investigated by the SIE method [21]. We discovered the particularity in the electric field distribution on the cross-section of the open

metamaterial square waveguide at $f = 95\,\text{GHz}$. We found the frequency range ($f = 105$–$115\,\text{GHz}$) where the losses were very small.

2.1. The Integral Representation of Solution to Maxwell's Equations

The Maxwell's equations for this boundary problem have been solved by the electrodynamically rigorous SIE method. This method attracts much attention due to its positive features. The shape of the cross-section of the investigated waveguide structure may be arbitrary (Fig. 1).

In Fig. 1, the contour L separates materials with different permittivities and permeabilities. We assume that the area S^- is the waveguide surrounding media. All the boundary conditions in our solution are satisfied. We present here our researches of the square waveguide which boundary surfaces are parallel to the x- and y-axes. At the boundary which is parallel to the x-axis we assume that $E_x^+ |L_x = E_x^- |_{Lx}$. At the boundary which is parallel to the y-axis, we assume that $E_y^+ |L_y = E_y^- |_{Ly}$, where contour L is composed from segments L_x and L_y. At all the boundaries we assume that $E_z^+ |_L = E_z^- |_L$. The analogical boundary conditions are satisfied for the magnetic field. The longitudinal components of the electric $E_z(\vec{r})$ and magnetic $H_z(\vec{r})$ fields at the contour L have the integral representation:

$$E_z(\vec{r}) = \int_L \mu_e(\vec{r}_s) H_0^{(2)}(k_\perp r') ds, \quad H_z(\vec{r}) = \int_L \mu_h(\vec{r}_s) H_0^{(2)}(k_\perp r') ds, \quad (1)$$

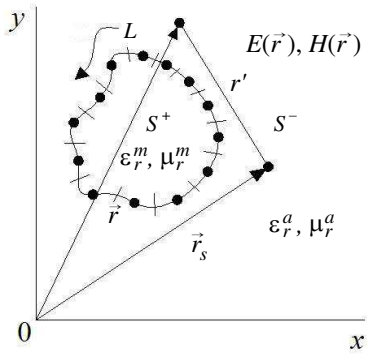

Figure 1. Geometry of an arbitrary cross-section rod waveguide and the SIE method notations.

where $H_0^{(2)}$ is the Hankel function of the zeroth order and the second kind. Here, the magnitude s is the *arc* abscissa, and ds is an element of contour L. The magnitudes $\mu_h(\vec{r}_s)$ and $\mu_e(\vec{r}_s)$ are the unknown functions satisfying the Höder condition [21]. We apply the Krylov-Bogoliubov method whereby the contour is divided into n segments and the integration along a contour L is replaced by a sum of integrals over the segments. The expressions of all electric field components are presented below.

The longitudinal components of the electric field for the area S^+ and S^- are:

$$\begin{aligned} E_z^+ &= \sum_{j=1}^{n} \mu_e^+(s_j) \int\limits_{\Delta L} H_0^{(2)}(k_\perp^+ r')ds, \\ E_z^- &= \sum_{j=1}^{n} \mu_e^-(s_j) \int\limits_{\Delta L} H_0^{(2)}(k_\perp^- r')ds. \end{aligned} \tag{2}$$

After substitution of the longitudinal field components (2) in the transverse component formulae [22], we obtain the expressions at the contour points:

$$\begin{aligned} (E_x)^+ &= -\frac{2\mu_0\mu_r^m\omega\cos\theta}{\left(k_\perp^+\right)^2}\mu_h^+(s_j) \\ &\quad -V_+\left[k_\perp^+\sum_{j=1}^{n}\left(\mu_h^+(s_j)\right)\int\limits_{\Delta L} H_1^{(2)}(k_\perp^+ r')\frac{y_S-y_0}{r'}ds\right] \\ &\quad +Q_+\left[k_\perp^+\sum_{j=1}^{n}\left(\mu_e^+(s_j)\right)\int\limits_{\Delta L} H_1^{(2)}(k_\perp^+ r')\frac{x_S-x_0}{r'}ds\right], \end{aligned} \tag{3}$$

$$\begin{aligned} (E_x)^- &= \frac{2\mu_0\mu_r^a\omega\cos\theta}{\left(k_\perp^-\right)^2}\mu_h^-(s_j) \\ &\quad -V_-\left[k_\perp^-\sum_{j=1}^{n}\left(\mu_h^-(s_j)\right)\int\limits_{\Delta L} H_1^{(2)}(k_\perp^- r')\frac{y_S-y_0}{r'}ds\right] \\ &\quad +Q_-\left[k_\perp^-\sum_{j=1}^{n}\left(\mu_e^-(s_j)\right)\int\limits_{\Delta L} H_1^{(2)}(k_\perp^- r')\frac{x_S-x_0}{r'}ds\right], \end{aligned} \tag{4}$$

$$
\begin{aligned}
(E_y)^+ &= -\frac{2\mu_0\mu_r^m\omega\cos\theta}{\left(k_\perp^+\right)^2}\mu_h^+(s_j) \\
&\quad -Q_+\left[k_\perp^+\sum_{j=1}^{n}\left(\mu_e^+(s_j)\right)\int\limits_{\Delta L}H_1^{(2)}(k_\perp^+r')\frac{y_s-y_0}{r'}ds\right] \\
&\quad -V_+\left[k_\perp^+\sum_{j=1}^{n}\left(\mu_h^+(s_j)\right)\int\limits_{\Delta L}H_1^{(2)}(k_\perp^+r')\frac{x_s-x_0}{r'}ds\right], \qquad (5) \\
(E_y)^- &= \frac{2\mu_0\mu_r^a\omega\cos\theta}{\left(k_\perp^-\right)^2}\mu_h^-(s_j) \\
&\quad -Q_-\left[k_\perp^-\sum_{j=1}^{n}\left(\mu_e^-(s_j)\right)\int\limits_{\Delta L}H_1^{(2)}(k_\perp^-r')\frac{y_s-y_0}{r'}ds\right] \\
&\quad -V_-\left[k_\perp^-\sum_{j=1}^{n}\left(\mu_h(s_j)\right)-\int\limits_{\Delta L}H_1^{(2)}(k_\perp^-r')\frac{x_s-x_0}{r'}ds\right], \qquad (6)
\end{aligned}
$$

where $\chi_+ = i\varepsilon_0\varepsilon_r^m\omega\Big/\left(k_\perp^+\right)^2$, $\chi_- = i\varepsilon_0\varepsilon_r^a\omega\Big/\left(k_\perp^-\right)^2$, $V_+ = i\mu_0\mu_r^m\omega\Big/\left(k_\perp^+\right)^2$, $V_- = i\mu_0\mu_r^a\omega\Big/\left(k_\perp^-\right)^2$, $Q_+ = ih\Big/\left(k_\perp^+\right)^2$, $Q_- = ih\Big/\left(k_\perp^-\right)^2$, $h = h' - h''i$ is the complex longitudinal propagation constant where h' is the real part (phase constant), and h'' is the imaginary part (attenuation constant) of the value h. The field components and the values of the unknowns functions $\mu_h(s_j)$ and $\mu_e(s_j)$ are noted in the upper-right corner with the sign corresponding to different areas S^+ or S^-, i.e., the unknowns functions inside of waveguide are $\mu_e^+(s_j)$ $\mu_h^+(s_j)$ and outside of waveguide $\mu_e^-(s_j)$, $\mu_h^-(s_j)$. These functions at the same contour point are different for the field components in the areas S^+ and S^-, i.e., $\mu_{e,h}^+(s_j) \neq \mu_{e,h}^-(s_j)$. Magnitudes $k_\perp^+ = \sqrt{k^2\varepsilon_r^m\mu_r^m - h^2}$ and $k_\perp^- = \sqrt{h^2 - k^2\varepsilon_r^a\mu_r^a}$ are the transversal propagation constants of the metamaterial medium in the area S^+ and in the air area S^-, correspondingly (Fig. 1). Magnitudes $\varepsilon_r^m = \mathrm{Re}(\varepsilon_r^m) - \mathrm{Im}(\varepsilon_r^m)$ and $\mu_r^m = \mathrm{Re}(\mu_r^m) - \mathrm{Im}(\mu_r^m)$ are the complex permittivity and permeability of the metamaterial medium. Magnitudes ε_r^a and μ_r^a are the permittivity and permeability of air around the waveguide. The value $k = \omega/c$ is the wavenumber in air, $\omega = 2\pi f$, where f is an operating frequency. The contour L is divided into n segments, and the length of a segment is $\Delta L = L/n$

where the limits of integration in the formulas (2.6) are the ends of each segment ΔL. $H_1^{(2)}$ is the Hankel function of the first order and the second kind. The angle θ is equal to $g \cdot 90^\circ$ with g from 1 till 4 for rectangular contours in the formulae (3)–(6). The expressions for the magnetic field components are similar. The system of the algebraic equations obtained from the boundary conditions is homogeneous. The condition of solvability is obtained equalizing the determinant of the system to zero. The determinant is our dispersion equation. We have used the Müller's method to find the complex roots. The roots of the dispersion equation give the propagation constants of waveguide modes. After obtaining the propagation constants of the desired modes we can determinate the EM field of these modes (see formulae (2)–(6)). For the correct formulated problem the solution is one valued and stable with respect to small changes of the coefficients and contour form [21].

2.2. Numerical Investigations of Square Metamaterial Waveguide

The dispersion characteristics and 3D electric field distributions are presented here (Figs. 2–4). The values of ε_r^m and μ_r^m are different at every frequency [20]. The real part of the permittivity is always negative at the frequency range 75–115 GHz. The imaginary part of the permittivity is negative when $90 \leq f \leq 100$ GHz. The real part of the permeability is negative when $100 \leq f \leq 105$ GHz. The imaginary part of the permeability is always positive at the mentioned frequency

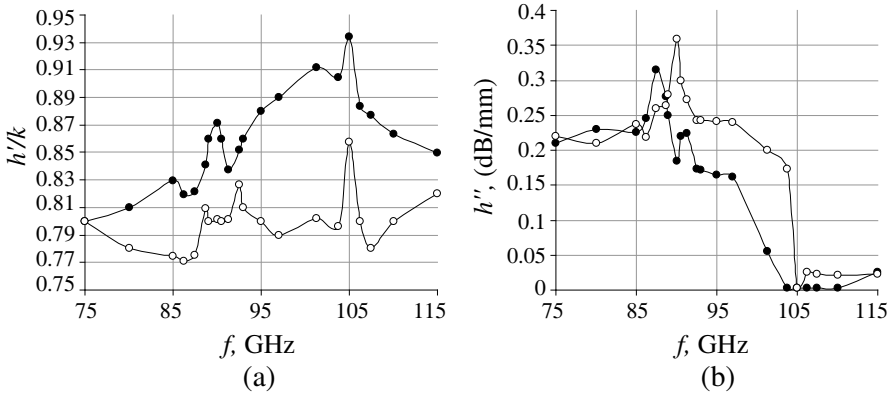

Figure 2. The dispersion characteristics of the metamaterial rectangular waveguide: (a) the dependence of the normalized phase constant, (b) the attenuation constant.

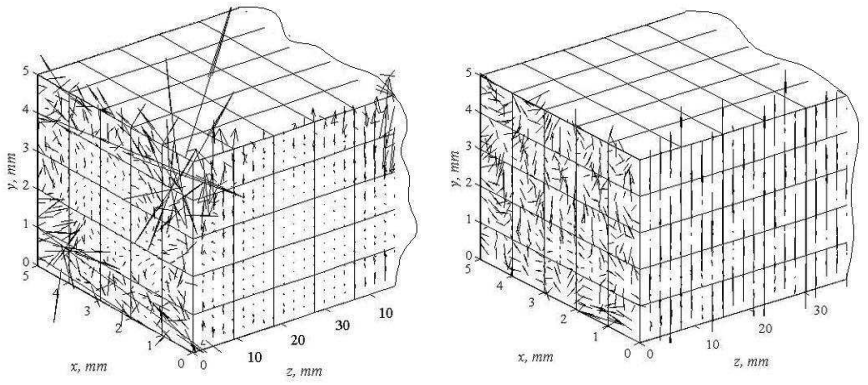

Figure 3. The 3D electric field distribution of the main mode propagating in the rectangular metamaterial waveguide: (a) $-f = 95\,\text{GHz}$, (b) $-f = 110\,\text{GHz}$.

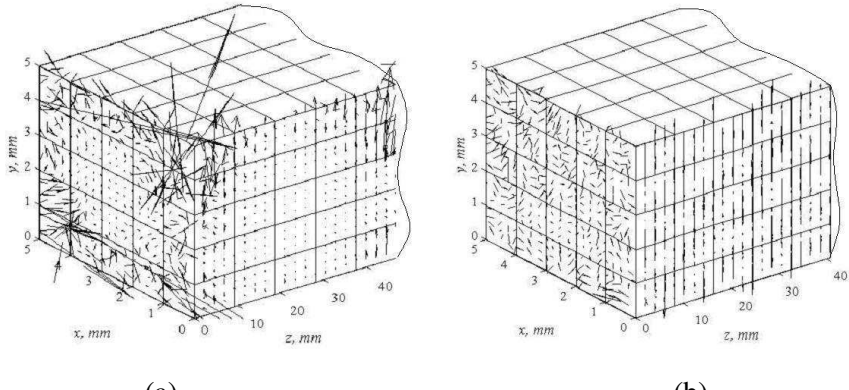

Figure 4. The 3D electric field distribution of the first higher mode propagating in the rectangular metamaterial waveguide: (a) $-f = 95\,\text{GHz}$, (b) $-f = 110\,\text{GHz}$.

range. The dependencies of complex longitudinal propagation constant $h = h' - h''i$ on the frequency is presented in Fig. 2. The main mode is denoted with points, and the first higher mode is denoted with circles.

In Fig. 2(a), we see dependencies of the normalized phase constant h'/k on the frequency, where $h' = 2 \cdot \pi/\lambda_w$ and λ_w is the wavelength of microwave in the metamaterial waveguide. The curves of the

main mode and the first higher mode are not smooth. We see that magnitudes $h'/k < 1$ for both modes (Fig. 2(a)). It means that the main and first higher modes are the fast waves. Fig. 2(b) shows the dependencies of the waveguide losses h'' on the frequency. We see that the values of the main and higher mode losses are commensurate, and the losses are not high in all frequency range. It is important to remark that the losses of the main modes are very small at the frequency range from 105 GHz to 115 GHz. This feature could be used in practice for the creation of feeder lines and specific devices that require low distortions in a signal transmission.

The 3D electric field distributions of the main mode at $f = 95$ GHz and 110 GHz are shown in Fig. 3. The metamaterial has $\varepsilon_r^m = -35 - 2.5i$ and $\mu_r^m = 2.25 + 0.25i$ at $f = 95$ GHz. And the metamaterial has $\varepsilon_r^m = -10.83 - 0.02i$ and $\mu_r^m = 0.5 - 0.01i$ at $f = 110$ GHz.

The metamaterial is an ENG medium at these frequencies. We see that the waveguide losses are relatively large at $f = 95$ GHz, and they are small at $f = 110$ GHz (Fig. 2(b)). In Fig. 3(a), we see that the electric field is very small in the center of the waveguide cross-section. The electric field concentrates near the waveguide border. Such distribution can be explained by the large loss at $f = 95$ GHz, and the EM wave does not deeply penetrate into the metamaterial.

In Tables 1 and 2, we demonstrate the values of complex EM field components of the main mode and the first higher mode at two frequencies. Based on the table data we can see that both modes on these frequencies are hybrid modes.

Table 1. The EM field components of the main mode at the point with coordinates $x = 4$ mm and $y = 4$ mm when $f = 95$ GHz and $f = 110$ GHz.

$f = 95$ GHz		
E_z [V/m]	E_x [V/m]	E_y [V/m]
$3.765 \cdot 10^{-1} - 6.411 \cdot 10^{-1}i$	$1.5099 - 2.1941i$	$-0.9943 + 1.9673i$
H_z [A/m]	H_x [A/m]	H_y [A/m]
$-3.39 \cdot 10^{-2} + 7.51 \cdot 10^{-2}i$	$-7 \cdot 10^{-4} + 1.1 \cdot 10^{-3}i$	$2.6 \cdot 10^{-3} - 3.9 \cdot 10^{-3}i$
$f = 110$ GHz		
E_z [V/m]	E_x [V/m]	E_y [V/m]
$-1.2766 \cdot 10^{-5}$ $-1.6592 \cdot 10^{-5}i$	$0.0134 + 0.0211i$	$-0.0291 + 0.0702i$
H_z [A/m]	H_x [A/m]	H_y [A/m]
$-3.0 \cdot 10^{-3} - 2.9 \cdot 10^{-3}i$	$1.3048 \cdot 10^{-4}$ $-3.0558 \cdot 10^{-4}i$	$5.9501 \cdot 10^{-5}$ $+1.0936 \cdot 10^{-4}i$

Table 2. The EM field components of the first higher mode at the point with coordinates $x = 4\,\text{mm}$ and $y = 4\,\text{mm}$ when $f = 95\,\text{GHz}$ and $f = 110\,\text{GHz}$.

$f = 95\,\text{GHz}$		
E_z [V/m]	E_x [V/m]	E_y [V/m]
$3.932 \cdot 10^{-1}$ $-6.181 \cdot 10^{-1}i$	$1.3730 - 1.8577i$	$-9.535 \cdot 10^{-1} + 1.6598i$
H_z [A/m]	H_x [A/m]	H_y [A/m]
$-3.20 \cdot 10^{-2}$ $+6.36 \cdot 10^{-2}i$	$-8 \cdot 10^{-4} + 1.4 \cdot 10^{-3}i$	$2.5 \cdot 10^{-3} - 3.4 \cdot 10^{-3}i$
$f = 110\,\text{GHz}$		
E_z [V/m]	E_x [V/m]	E_y [V/m]
$1.3083 \cdot 10^{-6}$ $-1.2678 \cdot 10^{-5}i$	$-4.6 \cdot 10^{-3} + 2.30 \cdot 10^{-2}i$	$-2.63 \cdot 10^{-2} + 4.31 \cdot 10^{-2}i$
H_z [A/m]	H_x [A/m]	H_y [A/m]
$-1.9 \cdot 10^{-3}$ $-2.4 \cdot 10^{-3}i$	$1.0715 \cdot 10^{-4}$ $-1.7759 \cdot 10^{-4}i$	$-2.7720 \cdot 10^{-5}$ $+1.0632 \cdot 10^{-4}i$

In Figs. 3(a)–4(a), we see that the electric field at $f = 95\,\text{GHz}$ for the main and first higher modes is concentrated near the metamaterial borders and that the strongest field is at two diagonal corners of the cross-section, i.e., at the right upper corner and the left bottom corner. There is a strong asymmetry of the electric field distribution on the perimeter of the waveguide. It happenes because at this frequency the real and imaginary parts of permittivity are negative and relatively large. The corners also have strong influence on the electric field distribution. Examining the field lines near the upper right corner (or the left bottom corner) we see that the electric field lines are directed clockwise or counter-clockwise to the right and left of the top corner. We will further see the very similar effect of the electric field asymmetry on the waveguide perimeter for the circular metamaterial waveguide.

In Figs. 3(b)–4(b), we see that the electric field distributions of the main and first higher modes have a more homogeneous picture in the waveguide cross-section at $f = 110\,\text{GHz}$. This happenes because the electric field penetrates deeper into the metamaterial at this frequency because the waveguide loss is small at $f = 110\,\text{GHz}$ (Fig. 2(b)). The projections of the vector electric fields on the waveguide sides are depicted along the waveguide (Figs. 3–4). The calculations of the electric fields were fulfilled at approximately 10000 points in every cross-section.

3. INVESTIGATIONS OF THE CIRCULAR METAMATERIAL WAVEGUIDE BY THE PARTIAL AREA METHOD

Here, the open metamaterial circular rod waveguide is investigated by the partial area formulae [19]. We discover the particularity in the electric field distribution on the cross-section of the open metamaterial circular waveguide at the operating frequency 95 GHz. We assume that this waveguide could be used as a narrowband filter at frequencies 102–102.5 GHz.

The representation of longitudinal components of the electric E_z^m and magnetic H_z^m fields that satisfy Maxwell's equations in the metamaterial medium is in the form:

$$E_z^m = A_1 J_m\left(k_\perp^+ r\right)\exp(im\varphi), \quad H_z^m = B_1 J_m\left(k_\perp^+ r\right)\exp(im\varphi), \quad (7)$$

where A_1, B_1 are unknown arbitrary amplitudes. J_m is the Bessel function of the m-th order. $k_\perp^+$ is the transverse propagation constant of the metamaterial medium. r is the radius of the circular metamaterial waveguide. m is the azimuthal index characterizing azimuthal variations of the field. φ is the azimuthal angle. The electric field E_z^a and magnetic field H_z^a components that satisfy Maxwell's equations in air are:

$$E_z^a = A_2 H_m^{(2)}\left(k_\perp^- r\right)\exp(im\varphi), \quad H_z^a = B_2 H_m^{(2)}\left(k_\perp^- r\right)\exp(im\varphi) \quad (8)$$

where A_2, B_2 are unknown arbitrary amplitudes. $H_m^{(2)}$ is the Hankel function of the m-th order and the second kind. $k_\perp^-$ is the transverse propagation constant of air medium. As far as the circular waveguide is researched in the cylindrical coordinate system we have to satisfy the boundary conditions only for two components of the electric field (E_φ, E_z) and the magnetic field (H_φ, H_z). After the substitution of expressions (7) and (8) in the transverse components expressed in terms of the longitudinal components [22] we obtain the expressions of all transverse EM field components. A further solution is carried out under the scheme of Section 2.1 of present work. The result of solution is the dispersion equation in the determinant form.

The circular metamaterial waveguide with $r = 2.5$ mm is researched. The dispersion characteristics and the 3D electric and magnetic field distributions are presented (see Figs. 5–9). The dispersion characteristics are shown in Fig. 5. The main mode is denoted with points, and the first higher mode is denoted with circles. In Fig. 5(a), we see that the normalized phase constants of the main and first higher modes are fairly flat and smooth and only have a one small protrusion at frequencies between 97 GHz and 102 GHz.

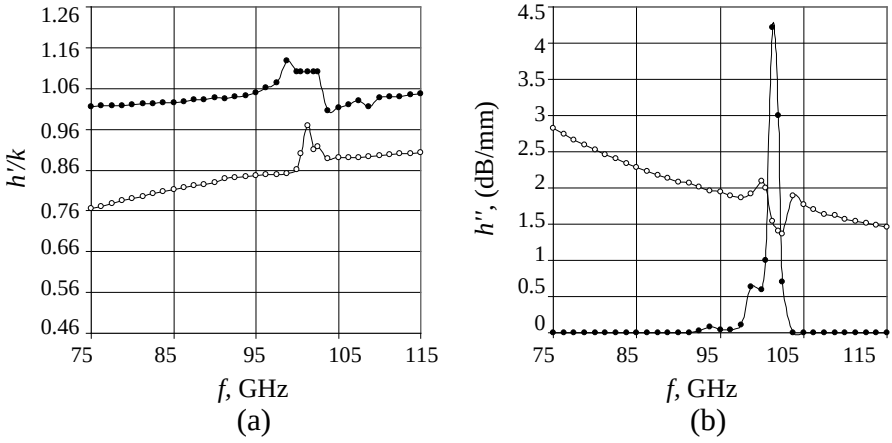

Figure 5. The dispersion characteristics of the metamaterial rectangular waveguide: (a) the dependence of the normalized phase constant, (b) the attenuation constant.

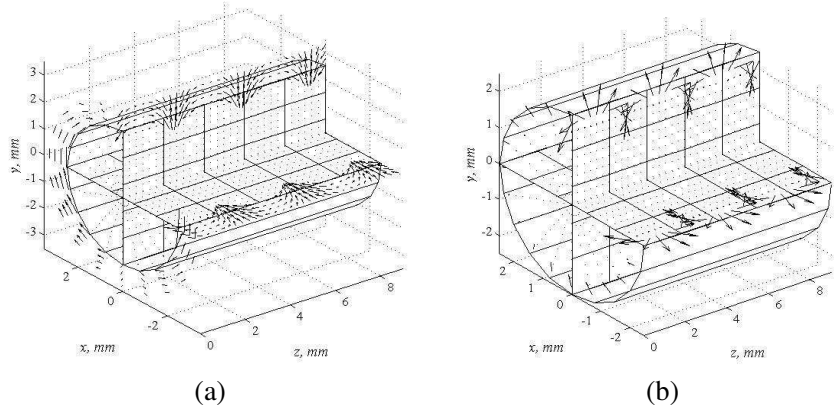

Figure 6. The 3D electric field distributions of the main mode at $f = 95\,\text{GHz}$: (a) the electric field strength lines outside the waveguide, (b) the 143 times zoomed electric field strength lines inside the waveguide.

There is a large peak of the main mode losses at frequency $f = 101.25\,\text{GHz}$. At this frequency metamaterial is DNG with $\varepsilon_r^m = -9.17 - 0.83i$ and $\mu_r^m = -0.75$. We see that losses of the main mode are very small at the frequency ranges 75–100 GHz and 102.5–115 GHz, while the losses of the first higher mode are significantly higher at the frequency ranges (Fig. 5(b)). Therefore, the investigated circular

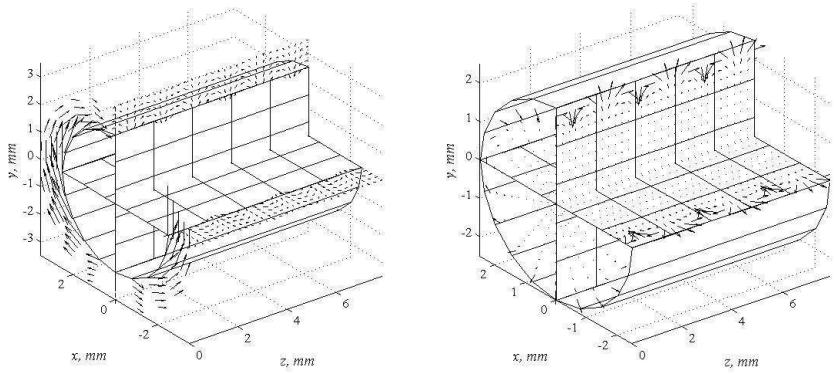

(a) (b)

Figure 7. The 3D electric field distributions of the main mode at $f = 110\,\text{GHz}$: (a) the electric field strength lines outside the waveguide, (b) the 14 times zoomed electric field strength lines inside the waveguide.

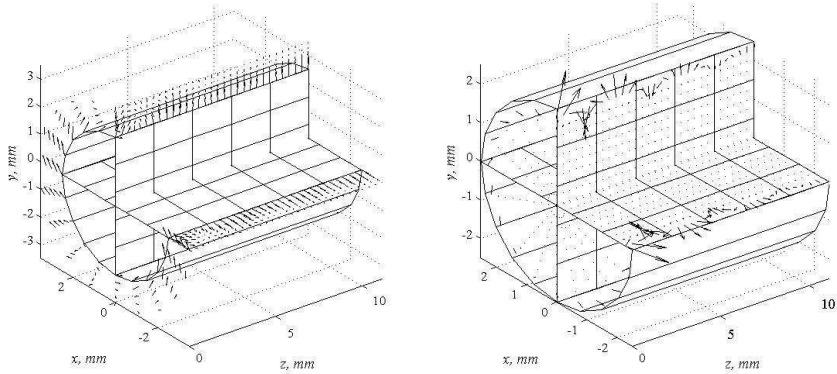

(a) (b)

Figure 8. The 3D electric field distributions of the first higher mode at $f = 95\,\text{GHz}$: (a) the electric field strength lines outside the waveguide, (b) the 143 times zoomed electric field strength lines inside the waveguide.

metamaterial waveguide can be used as a filter at the frequencies 100–102.5 GHz and as a one mode lossless waveguide at the frequency ranges 75–100 GHz and 102.5–115 GHz.

The 3D electric field distributions of the main mode are calculated at frequencies 95 GHz and 110 GHz (Figs. 6 and 7) as well as the first higher mode at the same frequencies (Figs. 8 and 9). The electric

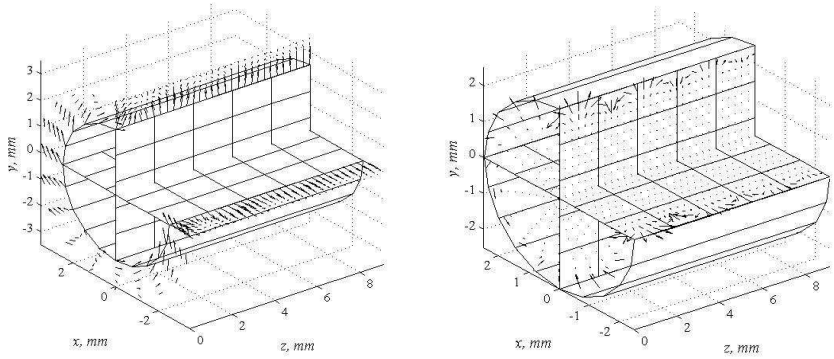

(a) (b)

Figure 9. The 3D electric field distributions of the first higher mode at $f = 110\,\text{GHz}$: (a) the electric field strength lines inside the waveguide, (b) the 14 times zoomed electric field strength lines outside the waveguide.

Table 3. The electromagnetic field components of the main mode at the point with coordinates $r = 2\,\text{mm}$, $\varphi = 45^\circ$ when $f = 95\,\text{GHz}$ and $f = 110\,\text{GHz}$.

$f = 95\,\text{GHz}$		
E_z [V/m]	E_x [V/m]	E_y [V/m]
$-2.5897 \cdot 10^{-5}$ $+2.7266 \cdot 10^{-}i$	$-2.8425 \cdot 10^{-5}$ $+1.9342 \cdot 10^{-5}i$	$4.5991 \cdot 10^{-6}$ $-3.3487 \cdot 10^{-5}i$
H_z [A/m]	H_x [A/m]	H_y [A/m]
$2.5111 \cdot 10^{-7}$ $-2.0158 \cdot 10^{-7}i$	$-2.3843 \cdot 10^{-8}$ $-2.8570 \cdot 10^{-1}i$	$2.5496 \cdot 10^{-6}$ $+1.8364 \cdot 10^{-1}i$
$f = 110\,\text{GHz}$		
E_z [V/m]	E_x [V/m]	E_y [V/m]
$0.0067 + 0.0067i$	$-0.0027 + 0.0027i$	$-7.8928 \cdot 10^{-4} - 7.8928 \cdot 10^{-1}i$
H_z [A/m]	H_x [A/m]	H_y [A/m]
$3.1409 \cdot 10^{-12}$ $-1.1109 \cdot 10^{-5}i$	$-3.3354 \cdot 10^{-6}$ $-3.3354 \cdot 10^{-6}i$	$7.1930 \cdot 10^{-5}$ $-7.1930 \cdot 10^{-5}i$

field inside the circular metamaterial waveguide is much smaller than outside of the waveguide. For this reason, we have increased (zoomed) the electric field strength lines inside waveguide in order to see them (Figs. 6(b)–9(b)). Because the metamaterial has a relatively large loss at 95 GHz in comparison with the metamaterial at 110 GHz, the electric field inside of waveguide is weaker at 95 GHz (see Tables 3 and

Table 4. The EM components of the first higher mode with coordinates at the point with coordinates $r = 2\,\text{mm}$, $\varphi = 45°$ when $f = 95\,\text{GHz}$ and $f = 110\,\text{GHz}$.

$f = 95\,\text{GHz}$		
E_z [V/m]	E_x [V/m]	E_y [V/m]
$1.6760 \cdot 10^{-4}$ $-3.3526 \cdot 10^{-4}i$	$3.5399 \cdot 10^{-5}$ $-1.2553 \cdot 10^{-5}i$	$-2.7112 \cdot 10^{-5}$ $-1.2042 \cdot 10^{-6}i$
H_z [A/m]	H_x [A/m]	H_y [A/m]
$-1.8851 \cdot 10^{-7}$ $-1.9128 \cdot 10^{-7}i$	$4.6704 \cdot 10^{-8}$ $+8.1377 \cdot 10^{-8}i$	$-3.1731 \cdot 10^{-6}$ $-1.4861 \cdot 10^{-6}i$
$f = 110\,\text{GHz}$		
E_z [V/m]	E_x [V/m]	E_y[V/m]
$-0.0053 - 0.0122i$	$0.0041 - 0.0021i$	$-3.2013 \cdot 10^{-4} + 9.6358 \cdot 10^{-4}i$
H_z [A/m]	H_x [A/m]	H_y[A/m]
$-1.0713 \cdot 10^{-5}$ $+9.0740 \cdot 10^{-7}i$	$7.1766 \cdot 10^{-6}$ $+9.3919 \cdot 10^{-6}i$	$-1.3582 \cdot 10^{-4}$ $+5.6938 \cdot 10^{-5}i$

4) compared to the inner electric field at 110 GHz. For this reason, we have zoomed the electric field strength lines at 95 GHz in the 143 times and at 110 GHz in the 14 time. The calculations of the electric fields are fulfilled at approximately 10000 points in every cross-section.

In Figs. 6–9, we see that the electric field is asymmetrical on the waveguide perimeter of the cross-section whilst the cross-section of the waveguide is a circle. We see that the most part of the electric field localizes outside of the waveguide. The outer electric field is the strongest when φ is 0 or π radians. The electric field lines are directed clockwise or counter-clockwise to the right and left of the points with φ equal to $\pi/2$ or $3\pi/2$ radians (Figs. 6(a)–9(a)). We see that at the points when the electric field outside of the metamaterial waveguide has the maximum value the field inside of the waveguide is minimal. In Figs. 6(b)–9(b), the maximum electric field inside the metamaterial waveguide is when φ is equal to $\pi/2$ or $3\pi/2$ radians. We can see that the electric field along the waveguide changes periodically (Figs. 6–9).

Comparing Figs. 6(a) and 7(a), we see that the main mode's electrical field at 110 GHz is twice as large and has a little different distribution in the longitudinal direction in comparison with the electrical field at 95 GHz. Since the losses of the main mode at frequencies 95 GHz and 110 GHz are small, the electric field amplitudes vary slightly in the longitudinal direction. Comparing Figs. 8 and 9, we also see that the larger is the electrical field outside of the waveguide the

smaller is the electrical field inside of waveguide. The last statement is true for all the investigated cases. The electric field amplitude of the first higher mode becomes smaller in longitudinal direction with increasing of coordinate z. We observe the wave attenuation (Figs. 8(b) and 9(b)). The attenuation happens because the losses of the first higher mode at 95 GHz and 110 GHz are large enough (Fig. 5(b)). The electrical field inside of the waveguide is very small at all frequencies. However, the observable electric field strength lines appear at the waveguide boundary.

We would like to draw attention to the fact that the feature of the asymmetric distribution of electric field in the cross-section of square and circular metamaterial waveguides at 95 GHz is very similar.

4. CONCLUSION

1. We present here two simple effective algorithms that let us analyze dispersion characteristics and 3D electric field distributions of the open square and circular metamaterial waveguides.

2. We discover that the electric field is concentrated at the metamaterial waveguide boundary and has the asymmetrical distribution on the waveguide perimeter at frequency 95 GHz when the metamaterial is a single negative matter with the relatively large negative complex permittivity. There are two areas on the perimeter of the square (Figs. 3(a), 4(a)) and circular (Figs. 6(a)–9(a)) waveguides where the electric field has the maximum value. These areas are shifted relative to each other on π radians.

3. We demonstrate here values of six EM field components in the point $x = 2 \cdot 10^{-3}$ m, $y = 2 \cdot 10^{-3}$ m of square waveguide and $r = 2 \cdot 10^{-3}$ m, $\varphi = 45^{\circ}$ of circular waveguide (Tables 1–4) for the main and first higher modes at two frequencies. We see that the hybrid modes propagate in the metamaterial waveguides.

4. We find that the losses of square metamaterial waveguide are very small at the frequency range from 105 GHz to 115 GHz.

5. We find that the circular waveguide could be used as a narrowband filter at frequencies 100–102.5 GHz. The waveguide is characterized by excellent properties, since the main mode has very small losses at the frequency ranges 75–100 GHz and 102.5–115 GHz, while the first higher mode has large losses at the same frequency ranges.

REFERENCES

1. Mirza, I. O., J. N. Sabas, S. Shi, and D. W. Prather, "Experimental demonstration of metamaterial based phase modulation," *Progress In Electromagnetics Research*, Vol. 93, 1–12, 2009.
2. Alu, A., N. Enghetal, A. Erentok, and R. W. Ziolkowski, "Single-negative, double-negative, and low-index metamaterials and their electromagnetic applications," *IEEE Antennas and Propag. Magazine*, Vol. 49, No. 1, 23–36, 2007.
3. Lagarkov, A. N., V. N. Semenenko, A. A. Basharin, and N. P. Balabukha, "Abnormal radiation pattern of metamaterial waveguide," *PIERS Online*, Vol. 4, No. 6, 641–644, 2008.
4. Xu, Z. X. and W. G Lin, "Controllable absorbing structure of metamaterial at microwave," *Progress In Electromagnetics Research*, Vol. 69, 117–125, 2007.
5. Chen, H., B.-I. Wu, and J. A. Kong, "Review of electromagnetic theory in left-handed materials," *Journal of Electromagnetic Waves and Applications*, Vol. 20, No. 15, 2137–2151, 2006.
6. Alù, A. and N. Engheta, "Guided modes in a waveguide filled with a pair of single-negative (SNG), double-negative (DNG), and/or double-positive (DPS) layers," *IEEE Trans. MTT*, Vol. 52, No. 1, 199–210, 2004.
7. Kim, K. Y., "Comparative analysis of guided modal properties of double-positive and double-negative metamaterial slab waveguides," *Radioengineering*, Vol. 18, No. 2, 117–123, 2009.
8. Wang, Z. J. and J. F. Dong, "Analysis of guided modes in asymmetric left-handed slab waveguides," *Progress In Electromagnetics Research*, Vol. 62, 203–215, 2006.
9. Li, C., Q. Sui, and F. Li, "Complex guided wave solutions of grounded dielectric slab made of metamaterials," *Progress In Electromagnetics Research*, Vol. 51, 187–195, 2005.
10. Mahmoud, S. F. and A. J. Viitanen, "Surface wave character on a slab of metamaterial with negative permittivity and permeability," *Progress In Electromagnetics Research*, Vol. 51, 127–137, 2005.
11. Lu, W. T., S. Savo, B. D. F. Casse, and S. Sridhar, "Slow microwave waveguide made of negative permeability metamaterials," *Microwave and Optical Technology Letters,* Vol. 51, No. 11, 2705–2709, 2009.
12. Liu, S.-H., C.-H. Liang, W. Ding, L. Chen, and W.-T. Pan, "Electromagnetic wave propagation through a slab waveguide of uniaxially anisotropic dispersive metamaterial," *Progress In*

Electromagnetics Research, Vol. 76, 467–475, 2007.

13. Zhou, H., Z. Pei, S. Qu, S. Zhang, J. Wang, Q. Li, and Z. Xu, "A planar zero-index metamaterial for directive emission," *Journal of Electromagnetic Waves and Applications*, Vol. 23, No. 7, 953–962, 2009.
14. Sabah, C. and S. Uckun, "Multilayer system of Lorentz/Drude type metamaterials with dielectric slabs and its application to electromagnetic filters," *Progress In Electromagnetics Research*, Vol. 91, 349–364, 2009.
15. Abdalla, M. A. and Z. Hu, "Multi-band functional tunable LH impedance transformer," *Journal of Electromagnetic Waves and Applications*, Vol. 23, 39–47, 2009.
16. Vafi, K., A. R. Maleki Javan, M. S. Abrishamian, and N. Granpayeh, "Dispersive behavior of plasmonic and metamaterial coating on achieving transparency," *Journal of Electromagnetic Waves and Applications*, Vol. 22, 941–952, 2008.
17. Si, L.-M. and X. Lv, "CPW-FED multi-band omni-directional planar microstrip antenna using composite metamaterial resonators for wireless communications," *Progress In Electromagnetics Research*, Vol. 83, 133–146, 2008.
18. Xi, S. and H. Chen, "Experimental confirmation of guidance properties using planar anisotropic left-handed metamaterial slabs based on s-ring resonators," *Progress In Electromagnetics Research*, Vol. 84, 279–287, 2008.
19. Nickelson, L., T. Gric, S. Asmontas, and R. Martavicius, "Electrodynamical analyses of dielectric and metamaterial hollow-core cylindrical waveguides," *Electronics and Electrical Engineering*, Vol. 82, No. 2, 3–8, 2008.
20. Penciu, R. S., M. Kafesaki, T. F. Gundogdu, E. N. Economou, and C. M. Soukoulis, "Theoretical study of left-handed behavior of composite metamaterials," *Photonics and Nanostructures — Fundamentals and Applications*, Vol. 4, 12–16, 2006.
21. Nickelson, L. and V. Shugurov, "*Singular Integral Equations' Method for the Analysis of Microwave Structures,* 348, VSP Brill Academic Publishers, Leiden, Boston, 2005.
22. Kong, J. A., *Electromagnetic Wave Theory,* 1016, EMW Publishing Cambridge, Massachusetts, USA, 2008.